nature materials

Supplementary information

https://doi.org/10.1038/s41563-026-02517-6

Quantum control of Hubbard excitons

In the format provided by the authors and unedited

Contents

S1 Quantifying the equilibrium Hubbard parameters

Starting from the reflectivity $R(\omega)$, we extract the optical conductivity from 0 to 5.8 eV by standard Kramers-Kronig (KK) analysis [1]. Figs. S1a-b show the normal-incidence reflectivity and optical conductivity for light polarized along the chains and at 295 K. To determine the extended Hubbard model (EHM) parameters (t, U, V) best capturing the optical response of Sr_2CuO_3, we fit the experimental optical conductivity $\sigma_1(\omega)$ to the analytical response of a 1D Mott insulator derived in Refs. [2, 3]. The reduced EHM optical conductivity $\omega\sigma_1(\omega)$ in the limit $U \gg t$ is:

$$\omega\sigma_1(\omega) = g_0 t^2 e^2 \frac{1}{\hbar}\left\{\theta(V-2t)\pi\left[1-\left(\frac{2t}{V}\right)^2\right]\delta(\omega-\omega_{\mathrm{CT}}) + \theta(4t-|\hbar\omega-U|)\frac{2t\sqrt{1-[\frac{\hbar\omega-U}{4t}]^2}}{V(\hbar\omega-\hbar\omega_{\mathrm{CT}})}\right\}, \quad (1)$$

where e is the electron charge, $\theta(x)$ the Heaviside function, and $g_0 = 2.65$ the zero-momentum form factor accounting for the spin degrees of freedom. In the "no-recoil" approximation, the optical response $\omega\sigma_1(\omega)$ is dominated by two $q = 0$ transitions: (i) a Hubbard exciton located at $\hbar\omega_{\mathrm{CT}} = U - V - 4t^2/V$ [4], and (ii) a particle-hole continuum (PH) of unbound holon-doublon excitations contributing a broad peak centered around U [3]. We fit the reduced optical conductivity (normalized to its maximum) up to 3.5 eV to the expression in Eq. (1). We use a genetic algorithm to determine the optimal values of U, V, and t. The best-fit EHM parameters are $t = 0.56$ eV, $U = 3.96$ eV, and $V = 1.17$ eV, which are used throughout the manuscript and are consistent with previous experimental findings [5].

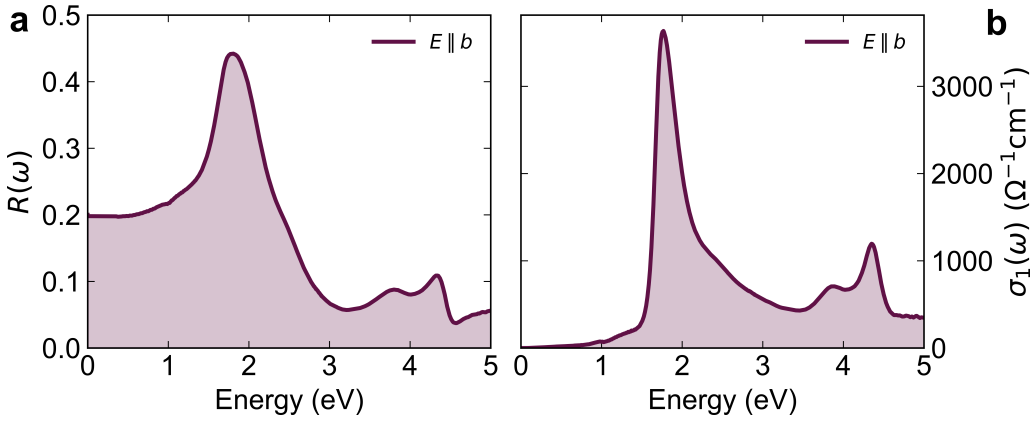

Fig. S1: Equilibrium optical properties of Sr_2CuO_3. a. Broadband reflectivity and **b.** optical conductivity of Sr_2CuO_3 at normal incidence and along the chain direction.

S2 NIR energy dependence of the THG renormalization

In this section, we present the time- and spectrally-resolved transient THG response upon varying NIR probe energy. Figure S2 displays the differential THG intensity $\Delta I_{3\omega}(\omega)/I_{3\omega}(\omega)$ for five NIR energies between 0.56 eV and 0.66 eV. The MIR pump energy is held fixed at 0.12 eV (28 THz), and the MIR fluence for each dataset is reported in the caption. Note that while here the data is acquired at the maximum achievable field strength at each MIR wavelength, the wavelength-dependent data reported in the main text is measured while maintaining the same MIR field strength at each NIR wavelength.

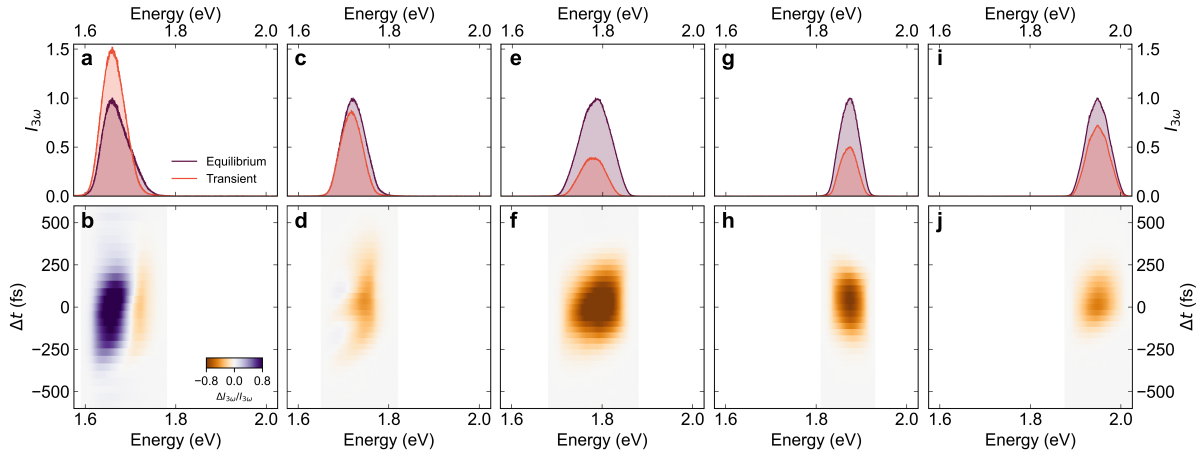

Fig. S2: NIR energy dependence of the THG renormalization. Time- and spectrally-resolved maps of the differential transient THG response. The driving frequency and the MIR peak electric field (E_{MIR}) are: 0.56 eV and 1.0 MV/cm in **a** and **b**, 0.58 eV and 1.5 MV/cm in **c** and **d**, 0.59 eV and 1.8 MV/cm in **e** and **f**, 0.63 eV and 1.7 MV/cm in **g** and **h**, and 0.66 eV and 1.3 MV/cm in **i** and **j**. Each of the panels in the upper row shows one-dimensional spectra at maximum pump-probe overlap ($\Delta t = 0$ fs) of the equilibrium (purple) and transient (orange) THG signal. The individual panels in the bottom row show the spectrally-resolved differential THG (normalized to the equilibrium signal) at different pump-probe delays (Δt).

S3 Dynamical THG renormalization of a light-driven extended Hubbard model

At equilibrium, Sr_2CuO_3 is described by an EHM Hamiltonian at half filling

$$\hat{H}_0 = -t\sum_{i,\sigma}^{L}\left(\hat{c}^{\dagger}_{i,\sigma}\hat{c}_{i+1,\sigma} + c.c.\right) + U\sum_{i}^{L}\hat{n}_{i,\uparrow}\hat{n}_{i,\downarrow} + V\sum_{i}^{L}\hat{n}_i\hat{n}_{i+1}, \tag{2}$$

where $\hat{c}^{\dagger}_{j,\sigma}$ ($\hat{c}_{j,\sigma}$) denotes the creation (annihilation) operator, $\hat{n}_{i,\sigma} = \hat{c}^{\dagger}_{j,\sigma}\hat{c}_{j,\sigma}$, and $\hat{n}_i = \hat{n}_{i,\uparrow} + \hat{n}_{i,\downarrow}$. U is the on-site Coulomb repulsion, while V is a repulsive nearest-neighbour Coulomb interaction. From Sec. S1, we fix the parameters to $U = 7.05t$ and $V = 2.08t$, with the hopping constant $t = 0.56$ eV. To simulate the exciton nonlinearity in presence of both NIR and MIR fields, we consider the combined

electric field $\vec{E}(t) = \vec{E}_{\mathrm{MIR}}(t) + \vec{E}_{\mathrm{NIR}}(t)$, where each $\vec{E}_{\Omega}(t)$ is described by the following envelope:

$$\vec{E}_{\Omega}(t) = \begin{cases} E^0_{\Omega} \cos(\Omega t) \cos^2\left(\frac{\Omega t}{2M_{\mathrm{cyc}}}\right), & \text{if } -M_{\mathrm{cyc}}T_{\Omega}/2 < t < M_{\mathrm{cyc}}T_{\Omega}/2 \\ 0, & \text{otherwise.} \end{cases} \tag{3}$$

M_{cyc} denotes the number of laser cycles and $T_{\Omega} = 2\pi/\Omega$ is the period of the NIR/MIR field. Fig. S3 shows calculations of the renormalized THG response of the Hubbard exciton on a $L = 8$ sites chain with open boundary conditions. We fix $M_{\mathrm{cyc}} = 10$ for both fields, $E^0_{\mathrm{MIR}} = 1.5$ MV/cm, $E^0_{\mathrm{NIR}} = 2.5$ MV/cm, and $\Omega_{\mathrm{MIR}} = 136$ meV (32.9 THz). The NIR energy is varied between 0.54 eV (130 THz)and 0.79 eV (190 THz). We note that larger chains (up to $L = 12$) consistently yield similar results, and the chain size only affects the position of the static THG peak due to the different energy level spacing upon varying L. We have verified that the results are robust against variations of the number of cycles, NIR/MIR field strengths, and MIR energy.

To obtain the nonlinear current, we introduce the coupling of the matter degrees of freedom with the vector potential of the laser field ($\vec{E}_{\Omega}(t) = -\partial_t \vec{A}_{\Omega}(t)$) via the Peierls substitution: $\hat{c}_{i,\sigma} \rightarrow \hat{c}_{i,\sigma} e^{-ia_0 e \int \vec{A}_{\Omega}(t)\cdot\vec{r}_i \mathrm{d}\vec{r}}$, where e is the elementary charge and a_0 is the lattice constant ($a_0 = 4.0$ Å). We then numerically solve the associated time-dependent Schrödinger equation assuming a system initially in the ground state of $\hat{H}_0$ to obtain the time-evolved wavefunction $|\Psi(t)\rangle$. The time-dependent current is given by the expectation value of the current operator:

$$\langle\Psi(t)|\,\hat{j}(t)\,|\Psi(t)\rangle = -iea_0 t\,\langle\Psi(t)|\sum_{i,\sigma}^{L}\left(e^{-ia_0 e\int \vec{A}_{\Omega}(t)\cdot\vec{r}_i d\vec{r}}\hat{c}^{\dagger}_{i,\sigma}\hat{c}_{i+1,\sigma} - \mathrm{H.c.}\right)|\Psi(t)\rangle\,. \tag{4}$$

Following Ref. [6], we first calculate the dipole acceleration $a(t) = -\mathrm{d}\,\langle\Psi(t)|\,\hat{j}(t)\,|\Psi(t)\rangle\,/\mathrm{d}t$ and obtain the harmonic spectrum through the Fourier transform of $a(t)$. Prior to that, the time-domain acceleration is multiplied by a Gaussian window function of the form: e^{-t^2/σ_G^2} with $\sigma_G = 53$ fs [7]. Typical equilibrium and transient THG spectra are presented in Fig. S3. In all ED THG calculations presented in this manuscript, we fix the NIR electric field at 2.5 MV/cm and the MIR at 1.5 MV/cm. We have confirmed that the dynamic effects observed in the ED calculations above remain valid in the infinite-size limit, free from finite-size effects. To this end, we performed infinite-size time-dependent density matrix renormalization group (i-trDMRG) calculations, which revealed the same qualitative features.

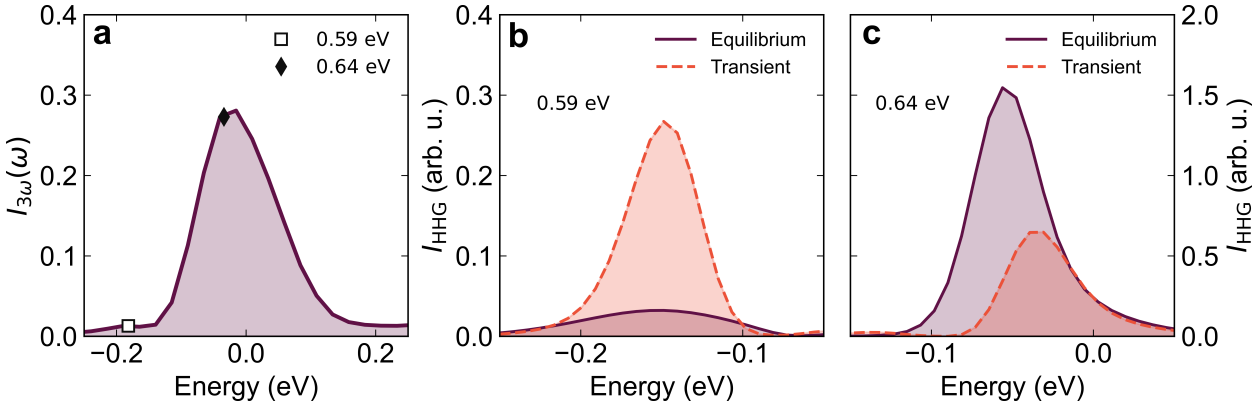

Fig. S3: ED calculation of the high harmonic response. Panel (a): Spectrally integrated static third-harmonic efficiency $I_{3\omega}^{\mathrm{eq}}$ at different NIR fundamental driving frequencies ω, shown as a function of the photon energy 3ω for a chain with $L = 8$ sites. Markers indicate two selected driving frequencies: one resonant to the Mott gap (0.64 eV) and one red-detuned (0.59 eV) with respect to it. Panels (b) and (c) show the equilibrium and transient THG spectra for the two selected drivers, 0.59 eV (b) and 0.64 eV (c), respectively. All curves are referenced to the energy of the odd excitonic state.

S4 Third-order Floquet susceptibility

S4.1 General Floquet analysis

The periodic driving of a many-body quantum state will lead to a dynamically renormalized nonlinearity which can be described through the Floquet formalism. Here, we explicitly derive the third-order susceptibility of a Floquet steady state of the EHM. Following Ref. [8], the induced polarization inside the material depends upon the expectation value of the dipole moment operator associated with the NIR-mediated transition:

$$\langle \tilde{\boldsymbol{p}} \rangle \equiv \langle \Psi(t) | \, \hat{\tilde{\mu}} \, | \Psi(t) \rangle \, . \tag{5}$$

In the above, $|\Psi(t)\rangle$ denotes the time-evolved wavefunction of the driven extended Hubbard chain under the action of the MIR pump. The Hamiltonian of this laser-driven system can be written as:

$$\hat{H}(t) = \hat{H}_0 + \hat{H}_d(t), \tag{6}$$

where $\hat{H}_0$ denotes the field-free EHM Hamiltonian and $\hat{H}_d(t) = -\hat{\tilde{\mu}} \cdot \vec{E}_{\mathrm{MIR}}(t)$ is the laser-matter interaction with the MIR field $\vec{E}_{\mathrm{MIR}}$ in the dipole approximation. If the laser field $\vec{E}_{\mathrm{MIR}}$ has a periodicity T ($T = 2\pi/\Omega$), then $\hat{H}_d(t) = \hat{H}_d(t+T)$ and we can expand $\Psi(t)$ in the basis of periodic Floquet functions $\{\Phi_\alpha\}$ as:

$$|\Psi(t)\rangle = \sum_\alpha b_\alpha e^{-i\varepsilon_\alpha t/\hbar} \, |\Phi_\alpha(t)\rangle \, , \tag{7}$$

where

$$|\Phi_\alpha(t+T)\rangle = |\Phi_\alpha(t)\rangle \tag{8}$$

and ε_α are the Floquet eigenenergies. The coefficients b_α are given by $b_\alpha = \langle\Phi_\alpha(t)|\Psi(t)\rangle$ and the Floquet eigenstates satisfy the orthonormality condition: $\langle\Phi_\alpha(t)|\Phi_\beta(t)\rangle = \delta_{\alpha\beta}$. $\Phi_\alpha(t)$ has the same periodicity as the MIR field and can be expanded in terms of the Floquet sidebands ϕ_α^m:

$$|\Phi_\alpha(t)\rangle = \sum_m e^{-im\Omega t}\,|\phi_\alpha^m\rangle\,. \tag{9}$$

The MIR-dressed chain is interrogated by the probe NIR field via:

$$\hat{\mathcal{H}}(t) = \hat{H}_d(t) + \hat{V}(t), \tag{10}$$

where

$$\hat{V}(t) = -\hat{\vec{\mu}}\cdot\tilde{\vec{E}}_{\mathrm{NIR}} = -\hat{\vec{\mu}}\cdot\sum_p \vec{E}_{\mathrm{NIR}}(\omega_p)e^{-i\omega_p t} \tag{11}$$

is the perturbation corresponding to the NIR electric field $\vec{E}_{\mathrm{NIR}}(t)$. To calculate the induced polarization $\langle\tilde{\boldsymbol{p}}\rangle$, we follow Ref. [9] and consider the time evolution operator:

$$\hat{U}(t,t_0) = \mathcal{T}e^{-i/\hbar\int_{-\infty}^{t}\hat{\mathcal{H}}(t')\mathrm{d}t'} = \hat{U}_d(t,t_0)\hat{S}(t,t_0), \tag{12}$$

where $\mathcal{T}$ denotes time ordering. $\hat{U}_d(t,t_0)$ is the part corresponding to the MIR driving and can be calculated as:

$$\hat{U}_d(t,t_0) = \sum_\alpha e^{-i\varepsilon_\alpha(t-t_0)/\hbar}\,|\Phi_\alpha(t)\rangle\,\langle\Phi_\alpha(t_0)|\,. \tag{13}$$

The operator $\hat{S}(t,t_0)$ incorporates the interaction with the probe light and is related to the perturbation $\hat{V}(t)$ in the interaction picture:

$$i\hbar\partial_t\hat{S}(t,t_0) = \hat{V}_I(t)\hat{S}(t,t_0), \tag{14}$$

where

$$\hat{V}_I(t) = \hat{U}_d^\dagger(t,t_0)\hat{V}(t)\hat{U}_d(t,t_0). \tag{15}$$

$\hat{S}(t,t_0)$ can be represented by a Dyson series expansion:

$$\hat{S}(t,t_0) = \mathbb{I} + \sum_{n=1}^{\infty}\left(\frac{-i}{\hbar}\right)^n\int^t \mathrm{d}t_1\int^{t_1}\mathrm{d}t_2\ldots\int^{t_{n-1}}\mathrm{d}t_n\hat{V}_I(t_1)\hat{V}_I(t_2)\ldots\hat{V}_I(t_n). \tag{16}$$

$\hat{U}(t,t_0)$ can be used to obtain the time-evolved $|\Psi(t)\rangle$ from the wavefunction at time t_0:

$$|\Psi(t)\rangle = \hat{U}(t,t_0)\,|\Psi(t_0)\rangle \equiv \hat{U}(t,t_0)\,|\Psi_g\rangle\,, \tag{17}$$

where

$$|\Psi_g\rangle = \sum_\alpha b_\alpha e^{-i\varepsilon_\alpha t_0/\hbar} |\Phi_\alpha(t_0)\rangle \tag{18}$$

is the MIR-dressed wavefunction prior to the interaction with the probe field. We now insert Eq. (17) in Eq. (5):

$$\langle\tilde{\boldsymbol{p}}\rangle = \langle\Psi_g| \hat{S}^\dagger(t,t_0)\hat{U}_d^\dagger(t,t_0)\hat{\tilde{\mu}}\hat{U}_d(t,t_0)\hat{S}(t,t_0)\,|\Psi_g\rangle\,. \tag{19}$$

and expand $\hat{S}(t,t_0)$ up to the third order:

$$\hat{S}(t,t_0) = \mathbb{I} + \hat{S}^{(1)}(t,t_0) + \hat{S}^{(1)}(t,t_0) + \hat{S}^{(3)}(t,t_0). \tag{20}$$

The third-order contribution to $\langle\tilde{\boldsymbol{p}}\rangle$ can be written as:

$$\begin{aligned}
\left\langle\tilde{\boldsymbol{p}}^{(3)}\right\rangle \;=\; & \langle\Psi_g|\,\hat{U}_d^\dagger(t,t_0)\,\hat{\tilde{\mu}}\,\hat{U}_d(t,t_0)\,\hat{S}^{(3)}(t,t_0)\,|\Psi_g\rangle + \\
& + \langle\Psi_g|\,\hat{S}^{(1)\dagger}(t,t_0)\,\hat{U}_d^\dagger(t,t_0)\,\hat{\tilde{\mu}}\,\hat{U}_d(t,t_0)\,\hat{S}^{(2)}(t,t_0)\,|\Psi_g\rangle + \\
& + \langle\Psi_g|\,\hat{S}^{(2)\dagger}(t,t_0)\,\hat{U}_d^\dagger(t,t_0)\,\hat{\tilde{\mu}}\,\hat{U}_d(t,t_0)\,\hat{S}^{(1)}(t,t_0)\,|\Psi_g\rangle + \\
& + \langle\Psi_g|\,\hat{S}^{(3)\dagger}(t,t_0)\,\hat{U}_d^\dagger(t,t_0)\,\hat{\tilde{\mu}}\,\hat{U}_d(t,t_0)\,|\Psi_g\rangle\,,
\end{aligned} \tag{21}$$

where:

$$\hat{S}^{(n)}(t,t_0) = \left(\frac{-i}{\hbar}\right)^n \int^t \mathrm{d}t_1 \ldots \int^{t_{n-1}} \mathrm{d}t_n \hat{V}_I(t_1)\ldots\hat{V}_I(t_n). \tag{22}$$

After a series of substitutions, we obtain the third-order susceptibility for a Floquet system in the frequency domain:

$$\begin{aligned}
\chi^{(3)}(-\omega_\sigma;\omega_p,\omega_q,\omega_r) \;=\; & \frac{1}{\hbar^3}\sum_{\alpha\delta}\sum_{pqr}\sum_{\gamma\mu\nu}\sum_{m_1l_1}\sum_{m_2l_2}\sum_{m_3l_3}\sum_{m_4l_4} b_\alpha^* b_\delta \exp\left\{i\left[\Omega_{\alpha\delta} - \omega_r - \omega_q - \omega_p\right]t\right\} \times \\
& \times \hat{\tilde{\mu}}_{\alpha\gamma}^{m_1,m_1+l_1}\hat{\tilde{\mu}}_{\gamma\mu}^{m_2,m_2+l_2}\hat{\tilde{\mu}}_{\mu\nu}^{m_3,m_3+l_3}\hat{\tilde{\mu}}_{\nu\delta}^{m_4,m_4+l_4} \times \\
& \times \left(\frac{1}{(\Omega_{\gamma\delta} - \Omega^{l_2l_3l_4} - \omega_r - \omega_q - \omega_p)(\Omega_{\mu\delta} - \Omega^{l_3l_4} - \omega_q - \omega_p)(\Omega_{\nu\delta} - \Omega^{l_4} - \omega_p)} + \right. \\
& + \frac{1}{(\Omega_{\gamma\alpha}^* - \Omega^{l_2l_3l_4} + \omega_r)(\Omega_{\mu\delta} - \Omega^{l_3l_4} - \omega_q - \omega_p)(\Omega_{\nu\delta} - \Omega^{l_4} - \omega_p)} + \\
& + \frac{1}{(\Omega_{\gamma\alpha}^* - \Omega^{l_2l_3l_4} + \omega_r)(\Omega_{\mu\alpha}^* - \Omega^{l_3l_4} + \omega_r + \omega_q)(\Omega_{\nu\delta} - \Omega^{l_4} - \omega_p)} + \\
& \left. + \frac{1}{(\Omega_{\gamma\alpha}^* - \Omega^{l_2l_3l_4} + \omega_r)(\Omega_{\mu\alpha}^* - \Omega^{l_3l_4} + \omega_r + \omega_q)(\Omega_{\nu\alpha}^* - \Omega^{l_4} + \omega_r + \omega_q + \omega_p)}\right),
\end{aligned} \tag{23}$$

where we have introduced the short-hand notations $\Omega^{l_1 l_2 \ldots l_k} = (l_1 + l_2 + \ldots + l_k)\Omega$ and $\Omega_{\alpha\beta} = \frac{1}{\hbar}(\varepsilon_\alpha - \varepsilon_\beta) - i\gamma$. Here, γ is a phenomenological broadening factor which we set to $\hbar\gamma = 0.06t$. Note that for third harmonic generation ($\chi^{(3)}(-3\omega;\omega,\omega,\omega)$), the above sum is restricted to the condition $l_1 + l_2 + l_3 + l_4 = 0$. The dressed dipole moment connecting individual Floquet sidebands is defined as $\hat{\tilde{\mu}}_{\alpha\gamma}(t) = \langle\Phi_\alpha(t)|\,\hat{\tilde{\mu}}\,|\Phi_\gamma(t)\rangle = \sum_{mn} e^{i(m-n)\Omega t}\,\langle\phi_\alpha^m|\,\hat{\tilde{\mu}}\,|\phi_\gamma^n\rangle = \sum_{mn} e^{i(m-n)\Omega t}\hat{\tilde{\mu}}_{\alpha\gamma}^{mn}$.

S4.2 Three-state model

In this section, we outline the phenomenological three-level system (3LS) model describing how the off-resonant MIR driving renormalizes the THG spectrum. Within this model, we consider only the ground state ($|0\rangle$) as well as the pair of even ($|g\rangle$; *gerade*) and odd ($|u\rangle$; *ungerade*) Hubbard excitons. Since the pump (0.12 eV) is far off-resonance with the charge gap ($\sim$ 1.8 eV), we neglect the Floquet dressing of the ground state by the drive. Further, we take the even and odd Mott excitons to be exactly degenerate with energy ϵ_{ex} and denote the dipole matrix element between even and odd exciton states along the chain direction by μ_{ug}. When driven by a *continuous-wave* (cw) oscillating electric field, the 3LS Hamiltonian ($\hat{H}_{\mathrm{3LS}}$) takes the following form:

$$\hat{H}_{\mathrm{3LS}}(t) = \epsilon_{ex}\,|u\rangle\,\langle u| + \epsilon_{ex}\,|g\rangle\,\langle g| + \mu_{ug}\mathcal{E}\,(|u\rangle\,\langle g| + |g\rangle\,\langle u|)\cos\Omega t, \tag{24}$$

where $\mathcal{E} \equiv E^0_{\mathrm{MIR}}$ is the pump field polarized along the chain direction and $\Omega \equiv \Omega_{\mathrm{MIR}}$ denotes its frequency. The ground state $|0\rangle$ lies at zero energy and hence does not enter explicitly in the Hamiltonian, as long as its AC Stark shift from highly off-resonant transitions [$\mu_{u,0}\,|u\rangle\,\langle 0| + \mathrm{h.c.}$] is negligible (see Methods). In other words, for simplicity we have set $\mathcal{E} \equiv E^0_{\mathrm{MIR}}$ and $\Omega \equiv \Omega_{\mathrm{MIR}}$.

In the Fourier space, the above Hamiltonian becomes:

$$\begin{aligned}\hat{H}^F_{\mathrm{3LS}} =& \epsilon_{ex}\,(|u\rangle\,\langle u| + |g\rangle\,\langle g|)\otimes\mathbb{I}_m - \sum_m m\mathbb{I}\otimes|m\rangle\,\langle m| \\ &+ \sum_m \frac{\mu_{ug}\mathcal{E}}{2}\,(|u\rangle\,\langle g| + |g\rangle\,\langle u|))\otimes(|m+1\rangle\,\langle m| + |m\rangle\,\langle m+1|)\,.\end{aligned} \tag{25}$$

While the *static* inversion symmetry is broken on a subcycle scale, the Hamiltonian $\hat{H}^F_{\mathrm{3LS}}$ is characterized by a *dynamical* inversion symmetry. In more detail, $\hat{H}^F_{\mathrm{3LS}}$ is invariant under time translation by half a period followed by inversion, that is, $\hat{H}^F_{\mathrm{3LS}}(t) = \hat{\Pi}\hat{H}^F_{\mathrm{3LS}}(t + \frac{T}{2})\hat{\Pi}$, where T is the MIR period and $\hat{\Pi}$ is the inversion operator. Similarly to the case of static inversion symmetry, we can choose the eigenstates to be either even or odd under the dynamical symmetry operation. Based on these considerations, we

write down the following *ansatz* for the dressed exciton eigenstates:

$$|\tilde{u}\rangle = \sum_m \phi^u_{2m} |u\rangle \otimes |2m\rangle + \phi^u_{2m+1} |g\rangle \otimes |2m+1\rangle \tag{26}$$

and:

$$|\tilde{g}\rangle = \sum_m \phi^g_{2m} |g\rangle \otimes |2m\rangle + \phi^g_{2m+1} |u\rangle \otimes |2m+1\rangle \,. \tag{27}$$

By inserting these eigenstates into the Fourier-transformed Hamiltonian (25), we find that the exciton energy does not change under intense pump driving and that $\phi^{u,g}$ satisfy the recursion relationship of Bessel functions. Based on these considerations, we derive the following expression for the dressed states:

$$|\tilde{u}\rangle = \sum_m J_{2m}\left(\frac{\mu_{ug}\mathcal{E}}{\hbar\Omega}\right) |u\rangle \otimes |2m\rangle + J_{2m+1}\left(\frac{\mu_{ug}\mathcal{E}}{\hbar\Omega}\right) |g\rangle \otimes |2m+1\rangle \tag{28}$$

and:

$$|\tilde{g}\rangle = \sum_m J_{2m}\left(\frac{\mu_{ug}\mathcal{E}}{\hbar\Omega}\right) |g\rangle \otimes |2m\rangle + J_{2m+1}\left(\frac{\mu_{ug}\mathcal{E}}{\hbar\Omega}\right) |u\rangle \otimes |2m+1\rangle \,. \tag{29}$$

With these states, we calculate the THG intensity using Eq. (23) with a focus on the contribution from the term corresponding to the three-photon resonance:

$$\chi^{(3)}(-3\omega;\omega,\omega,\omega) \;\propto\; \sum_n \frac{\left[J_n\left(\frac{\mu_{ug}\mathcal{E}}{\hbar\Omega}\right)\right]^2 \mu^2_{ug}\mu^2_{0u}}{(\epsilon_{ex}/\hbar + n\Omega - 3\omega - i\gamma)(\epsilon_{ex}/\hbar + n\Omega - 2\omega - i\gamma)(\epsilon_{ex}/\hbar + n\Omega - \omega - i\gamma)}, \tag{30}$$

where $\mu_{u0} \equiv \langle u|\hat{\mu}_b|0\rangle$ is the dipole matrix element between the equilibrium ground state and the undressed odd exciton.

S4.2.1 Rabi oscillations

The Floquet solution for the two-level system comprised of degenerate even and odd Hubbard excitons can be understood as a strong-coupling limit of the quantum-optical Rabi Hamiltonian. In atomic settings, the light-matter coupling $g = \vec{\mu}_{eg} \cdot \vec{E}$ for dipole-active transitions between two ground ($|g\rangle$) and excited states ($|e\rangle$) is much smaller than their energy difference Δ_{eg}. Consequently, a rotating-wave approximation is well-justified near resonance $\hbar\omega \approx \Delta_{eg}$ and the atomic state occupation oscillates with a Rabi frequency $\hbar\Omega_{\text{Rabi}} \approx \sqrt{g^2 + (\hbar\omega - \Delta_{eg})^2}$. The time evolution of a state initialized as $|g\rangle$ is shown in the top Bloch sphere of Fig. S4(a). The maximum overlap squared with the $|e\rangle$ state for a nearly resonant drive is $g^2/\hbar^2\Omega^2_{Rabi} \approx 1 - \delta^2/g^2$, where $\delta = \Delta_{eg} - \hbar\omega$. Hence, the oscillation amplitude is set by the detuning of the pump from resonance. Importantly, this phenomenology relies on the rotating wave approximation,

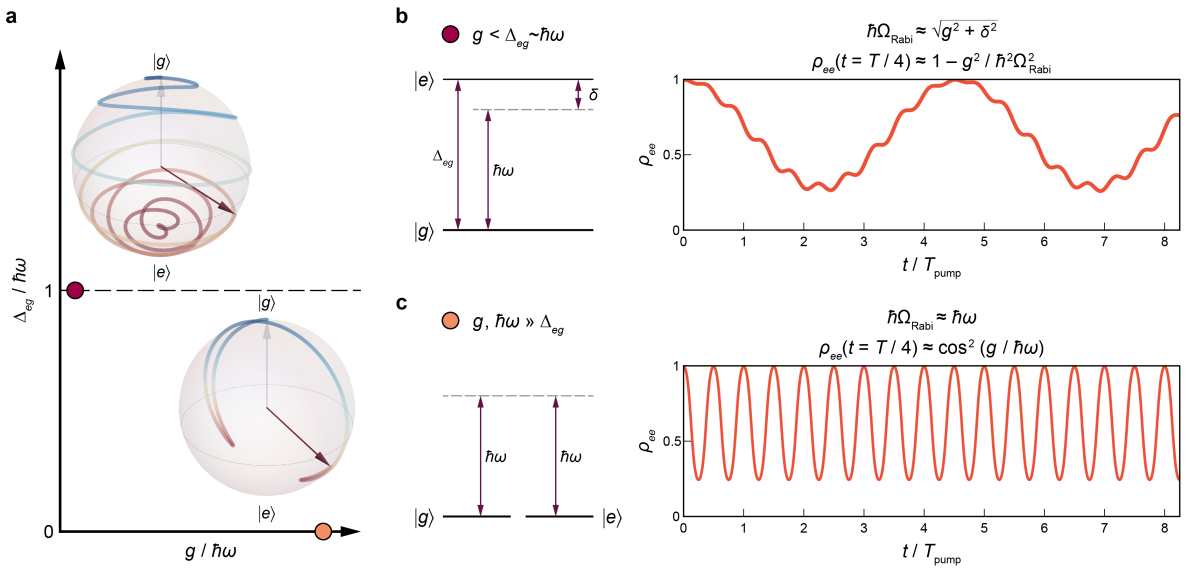

Fig. S4: Rabi oscillations in the strong-coupling limit for degenerate states $|e\rangle$, $|g\rangle$. Comparison between conventional quantum-optical Rabi problem (panel (a) top and panel (b)) and strong-coupling Rabi problem for a degenerate two-level system (panel (a) bottom and panel (c)). In the quantum-optical Rabi problem, characterized by a near-resonant driving field $\hbar\omega \sim \Delta_{eg}$ and weak light-matter coupling g, the $|e\rangle$ state population oscillates with a Rabi frequency $\Omega_{\mathrm{Rabi}} \approx g$. In contrast, in the Rabi problem relevant for driven Hubbard excitons, the light-matter coupling strength g becomes comparable to the pump frequency $\hbar\omega$, which in turn greatly exceeds a vanishing exciton splitting $\Delta_{eg} \to 0$. Here, the Rabi frequency is pinned to the driving frequency $\Omega_{\mathrm{Rabi}} \approx \omega$, while the Rabi amplitude is determined by $g/\hbar\omega$. The Bloch-sphere trajectories are shown in the laboratory frame (not the rotating frame) in both cases. For the motion of degenerate excitons, we introduce a small level splitting to visualize the dynamics more clearly.

which is only valid for $g \ll \Delta_{eg}, \hbar\omega$. For larger light-matter coupling, the counter-rotating terms cannot be neglected and the rotating wave approximation breaks down.

In contrast, driven Hubbard excitons lie in the strong coupling regime. Here, the light-matter coupling g for driven Hubbard excitons considered in the main text becomes comparable to the pump frequency ω, which in turn is highly off-resonant from the dipole transition between the nearly-degenerate exciton states. Since the exciton splitting is negligible, the physics is entirely controlled by the dimensionless parameter $g/\hbar\omega$. In this limit, described in the main text, the Rabi frequency is pinned to the pump frequency $\Omega_{\mathrm{Rabi}} \approx \omega$ while the Rabi amplitude is set by the light-matter coupling strength $g/\hbar\omega$. This phenomenology stands in sharp contrast to the conventional Rabi-oscillation regime, where the Rabi frequency is fixed by the light–matter coupling g and the oscillation amplitude is governed by the detuning. The corresponding Bloch-sphere trajectories also differ markedly from the resonant limit, as shown in Fig. S4(a). Under resonant driving, the state rotates between the poles of the Bloch sphere with a pronounced azimuthal component. By contrast, in the strong-coupling limit the motion is largely confined to the polar angle for exactly degenerate states, deviating only slightly for the nondegenerate cases shown in Fig. S4(a).

S4.2.2 Extraction of the Bloch rotation angle

As discussed in greater detail in Sec. S4.3.1, the presence of the holon-doublon (HD) continuum renormalizes the bare exciton response expected from the three-state model. To extract the rotation angle from the driven holon-doublon third-harmonic spectrum, we follow the procedure outlined below. First, the exciton energy ϵ_{ex} is determined by identifying the energy of the main peak. Second, the effective dipole matrix element μ_{ug} is obtained by comparing the relative heights of the main peak and the side peak in the THG spectrum with the prediction of Eq. (30). Lastly, since μ_{u0} is an overall prefactor in Eq. (30), its value is chosen to ensure that the height of the main peak in the three-state THG matches that of the holon-doublon THG (see Fig. S5). The rotation angle depends solely on the effective value of μ_{ug}. Once this value is determined, the rotation on the Bloch sphere can be calculated using the exact solutions of the dressed exciton wavefunctions in Eqs. (29) and (28).

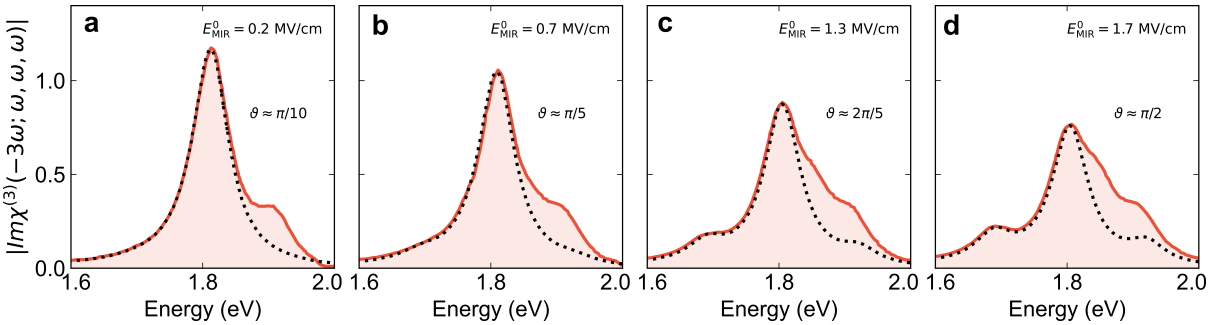

Fig. S5: Extraction of the Bloch rotation angle from the driven HD model. Comparison between imaginary third-order suceptibility obtained by solving the driven HD model (orange lines) and that predicted by the driven 3LS model with adjusted parameters (black dashed lines). The individual panels ((a)-(d)) correspond to different MIR pump strengths. The extracted Bloch angle rotation is indicated in each panel.

The presence of the continuum complicates the intracycle dynamics of the exciton wavefunction compared to a two-level Bloch-sphere system, due to mixing with unbound particle-hole states. Rather than a simple rotation around the Bloch sphere, the exciton evolves within a higher-dimensional Bloch sphere. This motion parallels the two-level system, but instead of oscillating between even and odd states, the exciton transitions between the even and odd parity sectors of the Hilbert space. Consequently, the cycle-averaged parity deviates from ± 1, reflecting the state trajectory around the higher-dimensional Bloch sphere, a many-body analog of the rotation angle. As discussed in Sec. S4.3.1, a change of basis can reduce this dynamics to an effective two-level system with renormalized parameters. Thus, the cycle-averaged parity can still be interpreted as an effective motion on a Bloch sphere.

S4.2.3 Simplified Bloch angle estimation

The Bloch spheres in the insets of Fig. 3 of the main text have been obtained using a simpler procedure based on a three-level system comprised of a ground state and two degenerate excited states, the latter being Floquet-dressed by the MIR field. Using the *ansatz* of Eqs. 26 and 27, we have:

$$\begin{aligned} |\tilde{u}\rangle &= \sum_m e^{2im\Omega t} J_{2m}\left(\frac{\mu_{ug}\mathcal{E}}{\hbar\Omega}\right)|u\rangle + e^{(2m+1)i\Omega t} J_{2m+1}\left(\frac{\mu_{ug}\mathcal{E}}{\hbar\Omega}\right)|g\rangle \\ &= \cos\frac{\vartheta}{2}|u\rangle + \sin\frac{\vartheta}{2}|g\rangle \qquad (31) \\ |\tilde{g}\rangle &= \sum_m e^{2mi\Omega t} J_{2m}\left(\frac{\mu_{ug}\mathcal{E}}{\hbar\Omega}\right)|g\rangle + e^{(2m+1)i\Omega t} J_{2m+1}\left(\frac{\mu_{ug}\mathcal{E}}{\hbar\Omega}\right)|u\rangle \\ &= \cos\frac{\vartheta}{2}|g\rangle + \sin\frac{\vartheta}{2}|u\rangle\,. \qquad (32) \end{aligned}$$

The Bloch angle is given by $\vartheta = 2\arccos\left[\sum_m J_{2m}\left(\frac{\mu_{ug}\mathcal{E}}{\hbar\Omega}\right)e^{2mi\Omega t}\right]$). The Bloch angle in the middle inset of Fig. 3 of the main text amounts to 121.66 deg. We used a MIR energy of 125 meV and the experimentally determined dipole moment of 7.37 Å [10]. We also assumed a sinusoidal field form with $E_{\mathrm{MIR}} = 1.8$ MV/cm and evaluated the Bloch angle at the maximum of the field, that is, at $t = T_{\mathrm{MIR}}/4$.

S4.3 Holon-Doublon model

The large optical nonlinearity of Mott insulating chains has traditionally been rationalized by modeling photoexcited states within a holon-doublon (HD) model [11, 12]. The spin degrees of freedom are effectively decoupled from the problem because of the inherent spin-charge separation of 1D systems. In the HD model, the ground state is a vacuum where all sites are singly-occupied and the excitations are doubly-occupied (doublons) and unoccupied (empty) sites (holons). Following [11], we define the equilibrium HD Hamiltonian as:

$$\hat{H}_{hd} = -t\sum_i\left(\hat{h}^\dagger_{i+1}\hat{h}_i + \hat{d}^\dagger_{i+1}\hat{d}_i + h.c.\right) - V\sum_{\langle i,j\rangle}\hat{h}^\dagger_i\hat{h}_i\hat{d}^\dagger_j\hat{d}_j + \frac{U}{2}\sum_i\left(\hat{h}^\dagger_i\hat{h}_i + \hat{d}^\dagger_i\hat{d}_i\right), \qquad (33)$$

alongside the condition that $\hat{h}^\dagger_i\hat{h}_i + \hat{d}^\dagger_i\hat{d}_i \leq 1$ for all sites i. Here, $\hat{h}^\dagger_i$ ($\hat{d}^\dagger_i$) is the operator that creates a holon (doublon) on site i. Note that we have made a gauge transformation, so that the hopping of both holons and doublons has the same sign. As we focus on the features near the excitonic peak, we constrain our analysis to the sector where $\sum_i \hat{h}^\dagger_i\hat{h}_i = \sum_i \hat{d}^\dagger_i\hat{d}_i = 1$. The HD model allows us to access larger system sizes than the extended Hubbard model, thus better capturing the effects from the continuum of unbound holon-doublon excitations.

To include the effects of the Floquet dressing, we couple the holon-doublon Hamiltonian to the electric field in the dipole gauge. This leads to:

$$\hat{H}^F_{hd}(t) = \hat{H}_{hd} + \hat{P}_{\text{dip}}\mathcal{E}(t), \tag{34}$$

where, as before, $\mathcal{E}(t) = \mathcal{E}\cos\Omega t$ is the MIR electric field (Ω is the angular frequency of the MIR pump) and $\hat{P}_{\text{dip}} = \sum_i ia(\hat{h}^\dagger_i\hat{h}_i - \hat{d}^\dagger_i\hat{d}_i)$ is the dipole operator along the chain ($a = ea_0$ is the dipole moment corresponding to an adjacent holon-doblon pair). We then use the extended-space formalism to find the Floquet eigenstates, including 40 sidebands to reach convergence. We then use formula (23) to calculate the THG spectrum of the system. Since the pump is far below resonance with respect to the charge gap, the equilibrium ground state is not appreciably dressed by the drive. As such, when applying Eq. (23), we assume that the system is in its ground state before the probe photoexcitation process.

Since the holon-doublon model is an effective description of the photoexcited states of the Hubbard model, the Hamiltonian parameters (t, U, V) are slightly renormalized from their corresponding values in the extended Hubbard model. The physics of the holon-doublon model is essentially controlled by V/t as U acts only as an overall chemical potential for the photoexcited states. To determine the appropriate parameter values, we use the methods described above to simulate the THG at different pump field strengths for various values of V/t and broadening factors $\hbar\gamma/t$ to determine the set of parameters that agree best with the experimental data. To compare with the experiment, we focus on the suppression of the main peak intensity. Upon varying V/t, we set U to a value such that the energy of the excitonic peak is fixed at $U - V - \frac{4t^2}{V} = 1.8$ eV. Lastly, because the dipole elements of the holon-doublon model are inherently arbitrary up to an overall scaling factor - and to account for any reflection, pump envelope shape effects, etc. - we include a rescaling factor between the simulated pump field strength and the experimental one ($E^{\text{exp}}_{\text{MIR}}/E^{\text{th}}_{\text{MIR}} = 1.85$). In the numerical results reported in the manuscript, we use $t = 0.56$ eV, $V/t = 2.4$, a broadening factor of $\hbar\gamma/t = 0.06$, and a chain length of 16 sites.

S4.3.1 Relation to the three-state model

The three-state model can be recovered by restricting the analysis to the Hubbard excitons. In this section, we show that one can take the Floquet Hamiltonian for the driven holon-doublon model and integrate out the holon-doublon continuum to arrive at a model that describes driven Hubbard excitons.

We choose to work in an eigenbasis of the dipole operator. We label each state as $|i, \mu\rangle \otimes |m\rangle$ where i is the site of the holon operator, μ denotes the dipole element of the state, and m is the Floquet replica index. The states with $\mu = \pm 1$ are excitons, whereas states with $|\mu| > 1$ correspond to unbound holon-doublon excitations.

If the hopping is turned off ($t = 0$), then $\hat{H}^F_{hd}$ can be solved exactly. Since each state is an eigenstate of $\hat{P}_{\text{dip}}$, $|i, \mu\rangle \otimes |m\rangle$ only mixes with states having the same values of i and μ. Therefore, the Hamiltonian is:

$$\begin{pmatrix} ... & & & \\ & E + \hbar\Omega & \frac{\mathcal{E}a\mu}{2} & 0 \\ & \frac{\mathcal{E}a\mu}{2} & E & \frac{\mathcal{E}a\mu}{2} \\ & 0 & \frac{\mathcal{E}a\mu}{2} & E - \hbar\Omega \\ & & & ... \end{pmatrix}, \tag{35}$$

where E is the equilibrium energy of the state ($E = U - V$ for the excitons and $E = U$ for the unbound states) and $\mathcal{E}$ is the field strength. Note that this Hamiltonian is just the three-state model, so we can diagonalize it exactly. Thus, the eigenstates of the above Hamiltonian become:

$$|i, \mu, m\rangle = \sum_n J_{n-m}\left(\frac{\mathcal{E}a\mu}{\hbar\Omega}\right)|i, \mu\rangle \otimes |n\rangle\,. \tag{36}$$

For $t \neq 0$ but $t \ll V$, we can perform a Schrieffer-Wolff transformation to build an effective Hamilton that only describes the excitons and their Floquet replicas. The basic picture is that a finite t lets the exciton break up into an unbound holon-doublon pair in the continuum and then recombine and come back to the exciton band. We wish to build an effective Hamiltonian which integrates out those processes. It is useful to define $\tilde{J}_m(x) = \sum_n J_{n-m}(2x)J_n(x)$ and

$$\tilde{t}_{m,\mu} = \frac{1}{2}t^2 \sum_l \tilde{J}_{l-m}\left(\frac{\mathcal{E}a\mu}{\hbar\Omega}\right)\tilde{J}_l\left(\frac{\mathcal{E}a\mu}{\hbar\Omega}\right)\left(\frac{1}{(l-m)\hbar\Omega + V} + \frac{1}{V + l\hbar\Omega}\right). \tag{37}$$

With these definitions, the effective Hamiltonian for the excitons becomes:

$$H_{eff} = U - V - \sum_{\langle i,j\rangle}\sum_{m,n}\sum_{\mu=\pm1}\tilde{t}_{m-n,\mu}\,|i, \mu, m\rangle\langle j, \mu, n| - \sum_{i,m,n}\sum_{\mu=\pm1}(2\tilde{t}_{m-n,\mu} - m\hbar\Omega\delta_{mn})\,|i, \mu, m\rangle\langle i, \mu, n|\,. \tag{38}$$

This Hamiltonian describes how excitons of each orientation (i.e, $\mu = -1$ for the "holon-doublon" configuration and $\mu = 1$ for the "doublon-holon" one) can hop between sites and also hop to different Floquet sidebands. Because this model is translationally invariant, it is natural to perform a Fourier

transform. This yields:

$$\hat{H}_{eff}(k) = U - V - 2\cos k \sum_{m,n} \sum_{\mu=\pm 1} \tilde{t}_{m-n,\mu} \left|k, \mu, m\right\rangle \left\langle k, \mu, n\right| - \sum_{i,m} \sum_{\mu=\pm 1} (2\tilde{t}_{m-n,\mu} - m\hbar\Omega\delta_{mn}) \left|k, \mu, m\right\rangle \left\langle k, \mu, n\right| . \tag{39}$$

Since the ground state has $k = 0$, we can work in the momentum sector where the Hamiltonian is:

$$\hat{H}_{eff}(k=0) = U - V - \sum_{i,m,n} \sum_{\mu=\pm 1} (4\tilde{t}_{m-n,\mu} - m\hbar\Omega\delta_{mn}) \left|k = 0, \mu, m\right\rangle \left\langle k = 0, \mu, n\right| . \tag{40}$$

Note that there are only two exciton states in this sector and, moreover, by taking even and odd superposition, we recover excitonic states which are even/odd under parity. When we consider these two excitons and the ground state, we recover the three-state model. Converting back into a time dependent Hamiltonian, we arrive at:

$$\hat{H}_{eff}(t) = \begin{pmatrix} 0 & 0 & 0 \\ 0 & \tilde{E}_{ex} + \tilde{X}_e(t) & \tilde{X}_o(t) \\ 0 & \tilde{X}_o(t) & \tilde{E}_{ex} + \tilde{X}_e(t) \end{pmatrix} , \tag{41}$$

where

$$\tilde{E}_{ex} = U - V - 4\tilde{t}_{0,+1} \qquad \tilde{X}_e(t) = -8 \sum_{i=1}^{\infty} \tilde{t}_{2i,+1} \cos\left(2i\Omega t\right) , \qquad \tilde{X}_o(t) = -8 \sum_{i=1}^{\infty} \tilde{t}_{2i-1,+1} \cos\left((2i-1)\Omega t\right) . \tag{42}$$

In the above, we have used that $\tilde{t}_{m,-1} = (-1)^m \tilde{t}_{m,+1}$ in order to combine terms. This is simply the original three-state model, but now there additional couplings which come from integrating out the continuum modes. Note that the expansion parameter for this Hamiltonian is t/V. In the experiment and the numerical calculations, $t/V \sim \frac{1}{2}$ which is outside of this perturbative regime. In light of this, the predictions from this effective Hamiltonian are useful in so far as they allow for a qualitative picture of how the pump renormalization process occurs.

The most important insight from this effective Hamiltonian is related to exciton energy. $\tilde{t}_0$ corresponds to the hopping in the same Floquet sideband and contributes to the overall energy of the exciton. For small fields, we can expand this as:

$$\tilde{t}_0 = \frac{t^2}{V} + \frac{1}{2} \frac{a^2 t^2}{V(V - \hbar\Omega)(V + \hbar\Omega)} \mathcal{E}^2 + ..., \tag{43}$$

where a is the dipole moment of the bare exciton. The first term is present at equilibrium while the second term originates from pump-induced processes which increase the hopping amplitude, redshifting the excitonic band edge.

S4.3.2 Coherent nature of the quantum state manipulation

In this section, we examine the coherence of the Floquet control protocol by analyzing the role of the exciton lifetime in its Floquet dressing. The exciton lifetime can be estimated from photodoping experiments that generate holon-doublon pairs across the Mott gap, yielding a value of approximately 2 ps [13], corresponding to more than 30 MIR cycles. Within the three-state model, we incorporate decoherence via a Lindblad operator, $J = \sqrt{\nu}\,|0\rangle\langle u|$, representing the radiative recombination of the odd exciton to the ground state [14, 15]. Here, $\nu/\hbar$ denotes the inverse exciton lifetime. Radiative decay of the even exciton is forbidden by dipole selection rules.

We simulate the pump-probe experiment using a three-level system with Lindblad recombination to account for the finite exciton lifetime. The exciton energy is fixed at $\epsilon_{ex} = 1.8$ eV, and the dipole matrix element is set to $\mu_{ug} = 7.37$ Å and $\mu_{u0} = 0.737$ Å [10]. The probe is modeled as a Gaussian pulse with a width of $2T$, where $T = 2\pi/\Omega$ is the the pump period, while the pump is treated as a continuous wave acting only on the excitonic states, a valid approximation given that the experimental MIR pump duration is much longer than that of the NIR probe. The probe field peaks at 0.9 MV/cm, and the pump field strength is set to 1.8 MV/cm. We numerically integrate the Lindblad master equation using a fourth-order Runge–Kutta method with a time step of $0.001T$, to obtain the time-dependent density matrix.

We first track the occupation of the odd excitonic state, $\langle O(t)\rangle = \mathrm{Tr}[\rho(t)O]$, where $O = |u\rangle\langle u|$, as shown in Fig. S6a. In the absence of both pump and recombination, the probe pulse alone populates the odd excitonic state, resulting in a long-lived occupation. When the system is driven, the occupation oscillates in time, reflecting the coherent rotation of the odd exciton into the even state under the pump field. This behavior is also evident in the Fourier transform of the exciton occupation shown in Fig. S6b. Unlike the equilibrium case, the driven system exhibits peaks at even integer multiples of the pump frequency. This is consistent with the exact solution (Eq. (28)), where the Fourier decomposition of the dressed exciton reveals that odd-parity components oscillate at even harmonics. Introducing a finite recombination rate reduces the spectral weight of these peaks, reflecting the damping of coherent oscillations due to the finite exciton lifetime.

Next, we investigate how the exciton lifetime affects the Floquet modulation of the THG spectrum. For probe energies between 0.54 and 0.68 eV, we compute the time-dependent expectation value of the

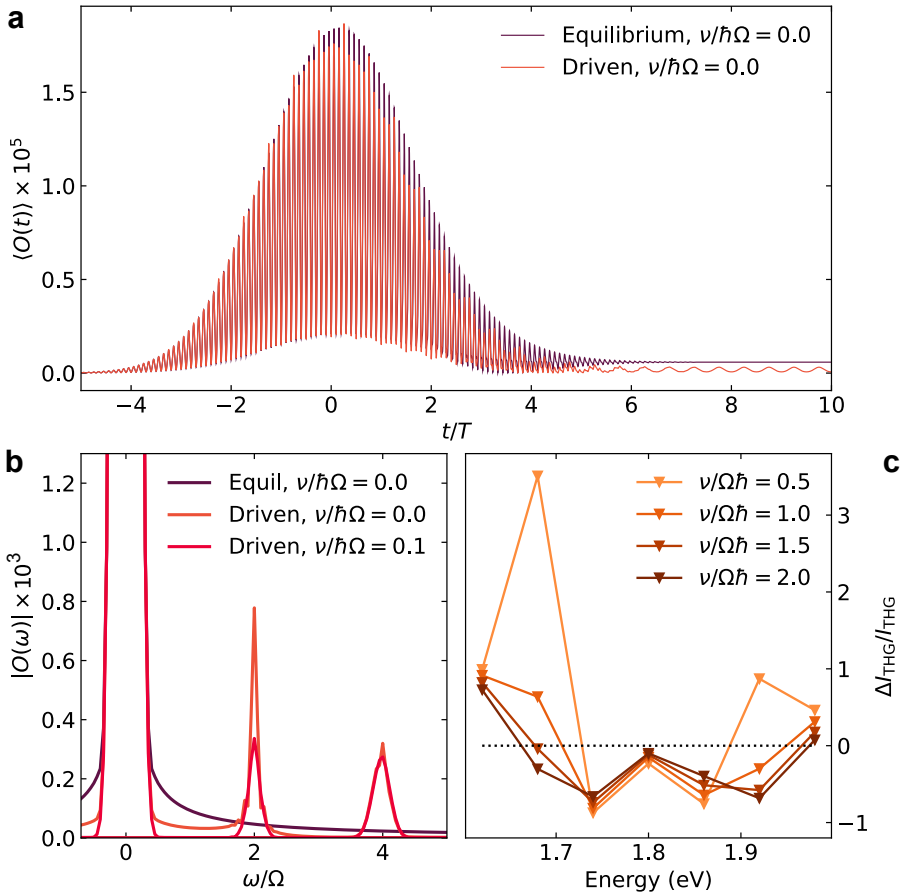

Fig. S6: Effect of exciton lifetime on Floquet dressing. a. Expectation value of the odd excitonic state occupation as a function of time for driven and undriven systems (without recombination effects).**b**. Fourier transform of the odd excitonic state occupation at equilibrium and under driving with and without exciton recombination **c**. Differential THG intensity change for various probe frequencies ω_p and recombination rates ν.

dipole operator, $\langle X(t)\rangle$, and extract its Fourier component near $3\hbar\omega_p$ for varying lifetimes. The intensity is determined by integrating the magnitude square of the spectral weight within ± 50 meV of $3\hbar\omega_p$. The change in intensity between the equilibrium and driven systems is shown in Fig. S6c. For all lifetimes, the main THG peak at $3\hbar\omega_p = \epsilon_{ex}$ is suppressed, although the degree of suppression decreases as the recombination rate increases. The most pronounced lifetime dependence appears at the sideband features at $3\hbar\omega_p = \epsilon_{ex} \pm \hbar\Omega$. Spectral weight emerges at these frequencies when the exciton inverse lifetime is shorter than the pump frequency, consistent with Floquet sideband formation. In contrast, when the inverse lifetime exceeds the pump frequency, this spectral weight is diminished. This reduction reflects the fact that Floquet sidebands require the exciton to persist over multiple pump cycles: if the exciton decays faster than one pump cycle, it cannot be coherently dressed by the drive. We conclude that under our experimental conditions the excitonic state is coherently rotated by the MIR pump and the amplitude of Floquet sidebands provides a clear indication for the degree of coherence of the driven state.

S4.3.3 Influence of V/t on the Floquet-driven third-harmonic signal

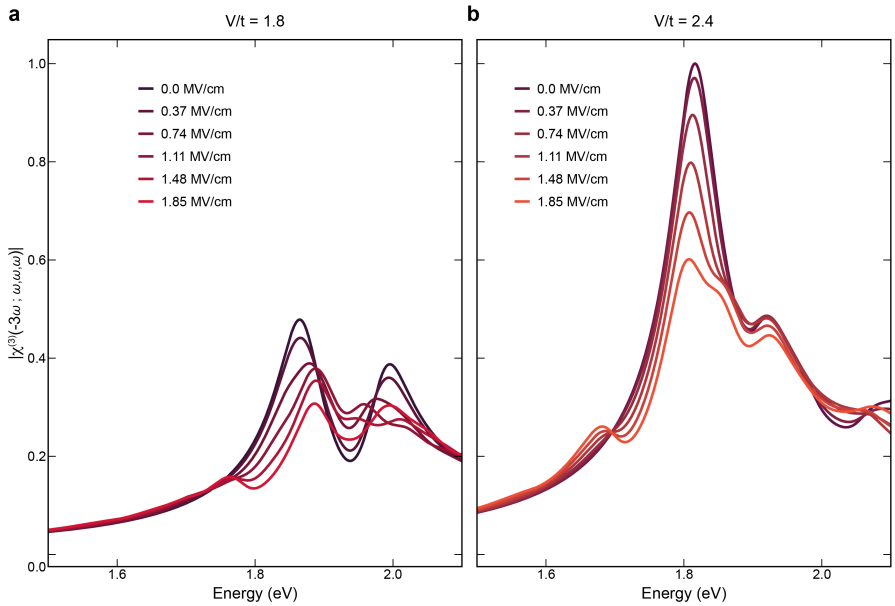

Fig. S7: Third-order nonlinearity for varying V/t ratio. MIR-Field-dependent third-order susceptibility of the holon–doublon model for $V < 2t$ (a) and $V > 2t$ (b). For $V < 2t$ there are no bound Hubbard excitons (as in Ca_2CuO_3), whereas for $V > 2t$ bound excitons are present (as in Sr_2CuO_3, our experiment).

Our holon–doublon model is, by construction, *agnostic* to whether the exciton is bound or unbound. When the binding energy is insufficient to form an exciton below the continuum (as in the closely-related compound Ca_2CuO_3 [12]), the pump field primarily induces Floquet dressing of unbound holon–doublon states rather than of an effective two-level system. In either case, the model fully accounts for the dressing of continuum states. To illustrate this, we contrast the Floquet-engineered third harmonic response in presence of unbound ($V/t = 1.8$) and bound ($V/t = 2.4$) excitons, Fig. S7. We normalize both spectra so that the maximum of the $V/t = 2.4$ response is unity. We note that the response for the unbound holon-doublon model ($V/t = 1.8$) is about half as strong as that of bound excitons ($V/t = 2.4$), in line with the experimental third harmonic intensity ratio of Ca_2CuO_3 and Sr_2CuO_3 [12]. For bound excitons (Fig. S7b), as the MIR field strengths increases, the peak primarily decreases in spectral weight while slightly red-shifting. In contrast, for unbound holon–doublon pairs (Fig. S7a), the primary effect is a renormalization of the continuum (appearing as multiple peaks due to finite-size and broadening effects) that shifts markedly because the Stark and Bloch–Siegert contributions no longer cancel, being mediated solely through continuum states. The in-gap Floquet sideband in this regime is also suppressed and broadened. Such behavior is inconsistent with the energy-dependent THG renormalization observed in our experiments and further supports Floquet dressing of Hubbard excitons as the origin of the nonlinear

response of MIR-driven Sr_2CuO_3. However, repeating the present experiment on Ca_2CuO_3 would enable directly probing the dressing of holon–doublon states in the continuum.

S5 Ruling out competition with sum-frequency generation

Owing to their strong optical nonlinearity, the Floquet-modulated third-harmonic generation (THG) of the driven Hubbard excitons is accompanied by emergent sum-frequency generation (SFG) peaks. We experimentally observe two SFG peaks at $2\hbar\omega_{\mathrm{NIR}} + \hbar\Omega_{\mathrm{MIR}} \approx 1.3$ eV and $4\hbar\omega_{\mathrm{NIR}} + \hbar\Omega_{\mathrm{MIR}} \approx 2.4$ eV, corresponding to third- and fifth-order nonlinear processes, respectively. Only odd-order nonlinearities are symmetry-allowed in this centrosymmetric compound, whereas fourth-order terms at the Floquet sideband energies $3\hbar\omega_{\mathrm{NIR}} \pm \hbar\Omega_{\mathrm{MIR}}$ are symmetry-forbidden.

To rule out the possibility that the observed THG suppression arises from competition with SFG processes, we perform two independent checks: (1) we confirm that SFG peaks appear not only when THG is suppressed but also when it is enhanced at the Floquet sidebands, and (2) we measure the SFG intensity as a function of the MIR driving field (see Fig. S8). Both SFG peaks increase in intensity under MIR excitation, regardless of whether the corresponding THG response increases or decreases as function of the NIR drive energy (Fig. S8a). This observation rules out a sole photon transfer from THG to SFG as the origin of the observed modulation.

Following Ref. [16], we further examine the fluence dependence of the SFG peaks at $4\hbar\omega_{\mathrm{NIR}} + \hbar\Omega_{\mathrm{MIR}}$ (Fig. S8b). If the fluence-dependent growth of the SFG signal is slower than that of the THG peak, then a redistribution of photons from THG to SFG processes cannot fully account for the THG peak modulation. We find that the SFG intensity exhibits a saturating or nonmonotonic trend, particularly pronounced at 0.57 eV, with a slower field-dependent growth than the THG signal well below 1 MV/cm. These findings are consistent with observations in the context of SHG processes in Ref. [16], where the second-order nonlinearity is Floquet modulated, and indicate that the nonlinear susceptibility $\chi^{(3)}(\omega)$ is directly modulated by the MIR field.

The breakdown of quadratic scaling of the SFG intensity at these field strengths implies that Floquet effects are essential to understanding the modulation of optical nonlinearities. The SFG arises from a fifth-order process involving four probe photons and one pump photon, such that $\chi^{(5)}_{SFG} \propto E_{\mathrm{MIR}}$ and the intensity is expected to scale as E^2_{MIR}. The observed deviation from this scaling already below 1 MV/cm indicates that higher-order processes contribute at a comparable level and cannot be neglected.

We now theoretically estimate the field strength at which the SFG and THG intensity responses begin to diverge. At low pump fluence, the differential THG intensity can be expanded in the pump field,

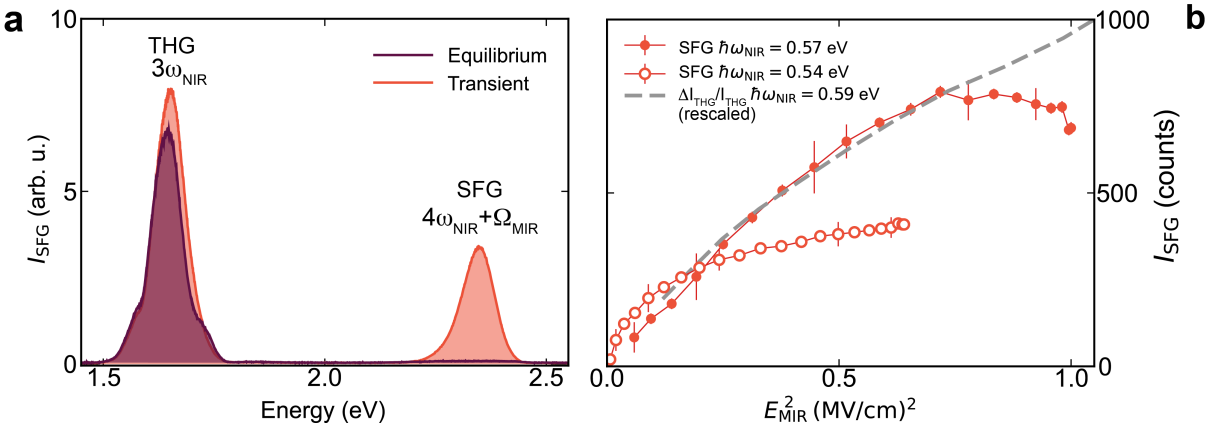

Fig. S8: Fifth-order sum-frequency generation. a. Third-harmonic ($3\hbar\omega_{NIR}$) and fifth-order SFG spectra ($4\hbar\omega_{NIR} + \hbar\Omega_{MIR}$) of a 0.54 eV NIR probe at equilibrium (purple) and after a 0.12 eV pump (orange, $\Delta t = 0$ fs, 0.8 MV/cm field strength). **b**. Driving field dependence of the SFG process at selected probe energies and comparison with rescaled absolute value of the THG suppression.

and the modification of $\chi^{(3)}$ can be attributed to a fifth-order process involving two pump photons. However, at higher field strengths, contributions from higher-order terms lead to deviations from this $\chi^{(5)}$ behavior. In this regime, the change in $\chi^{(3)}$ reflects a coherent renormalization induced by the drive, arising from the resummation of nonlinear optical processes to all orders in the pump field, as captured by Floquet theory. In the three-state model, the peak THG intensity under midinfrared irradiation scales as $J_0\left(\frac{\mu_{ug}\mathcal{E}}{\hbar\Omega}\right)^4$ where $\mathcal{E}$ is the MIR field, see Eq. (23). To leading order in the pump, the THG peak suppression goes as

$$\frac{\Delta I_{peak}}{I_{peak,eq}} = 1 - J_0\left(\frac{\mu_{ug}\mathcal{E}}{\hbar\Omega}\right)^4 = \left(\frac{\mu_{ug}\mathcal{E}}{\hbar\Omega}\right)^2 + \mathcal{O}(\mathcal{E}^4). \tag{44}$$

We define the breakdown of this perturbative limit when higher-order corrections (those at $\mathcal{E}^4$ or higher) account for 10% or more of the total THG suppression, that is when

$$\frac{|\Delta I_{\text{peak}}/I_{\text{peak,eq}} - (\frac{\mu_{ug}\mathcal{E}}{\hbar\Omega})^2|}{\Delta I_{\text{peak}}/I_{\text{peak,eq}}} = 0.1 \tag{45}$$

The equation is satisfied when $\mu_{ug}\mathcal{E}/\hbar\Omega = 0.47$, corresponding to a suppression of $\Delta I_{\text{peak}}/I_{\text{peak,eq}} = 0.20$. Once the suppression of the THG peak exceeds 20%, a complete Floquet treatment becomes necessary and the response must be understood as a pump-induced renormalization of the equilibrium third-order nonlinearity. This crossover corresponds to $E_{\text{MIR}} = 0.7$–0.8 MV/cm in Fig. 4 of the main text, and is matched to the fields in Fig. S8 where the nonmonotonic behavior becomes apparent.

S6 Energy shift of the THG spectra

In addition to intensity changes, the transient THG exhibits subtle variations of its spectral content. We track the THG peak position as a function of MIR field strength (Fig. S9a). With the MIR photon

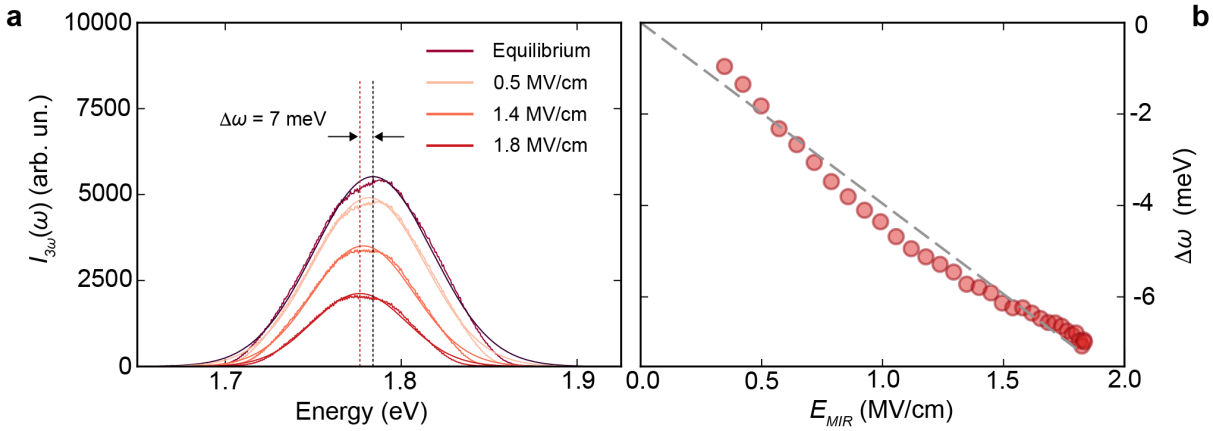

Fig. S9: Fluence dependence of the THG photon energy. a. Third harmonic spectra of a 0.59 eV NIR probe at equilibrium (purple) and after a 0.12 eV pump (orange, $\Delta t = 0$ fs) for selected field strengths. Spectra are fit to Gaussian profiles (solid lines), while the thin dashed lines indicate the THG peak position at equilibrium and at 1.8 MV/cm. **b**. THG peak position extracted from Gaussian fits as in panel **a.** Error bars are within the symbol size and the dashed grey line is a guide to the eye.

energy fixed at 0.12 eV, Gaussian fits to the THG spectra at each field reveal a small but measurable peak displacement. The THG peak shifts linearly with the MIR field, reaching 7 meV at the highest field strengths (Fig. S9b). Because the measured THG profile reflects a convolution of the incident NIR probe spectrum with the material's intrinsic third-order susceptibility, these measurements are sensitive to both relative shifts of the energy levels — arising from opposing optical Stark and Bloch-Siegert corrections [16, 17] — and a renormalization of the $\chi^{(3)}(-3\omega;\omega,\omega,\omega)$ magnitude. Given this convolution, the observed peak shift thus provides an upper bound for the actual shift of the excitonic levels. The modest magnitude of the observed THG shift, compared to reports in monolayer WS_2 and $MnPS_3$ where Floquet-engineered states are non-degenerate, is consistent with a response dominated by wave-function renormalization of $\chi^{(3)}(-3\omega;\omega,\omega,\omega)$ and near-cancellation of Stark and Bloch-Siegert shifts of the two near-degenerate excitons.

S7 Temperature dependence of the THG emission

To confirm that the THG renormalization arises from Floquet dressing of the excitons rather than relative shifts between ground and excited states, we also perform temperature-dependent equilibrium THG spectroscopy at selected near-infrared probe energies ($\hbar\omega = 0.56, 0.60$, and 0.64 eV), enabling a direct comparison with Fig. 4b of the main text. The equilibrium optical conductivity of Sr_2CuO_3 exhibits a redshift of the charge-transfer gap with increasing temperature (∼70 meV shift between 10 and 300 K) [4]. Hence, temperature-dependent THG measurements directly quantify how a redshifting absorption edge affects the frequency-dependent THG yield.

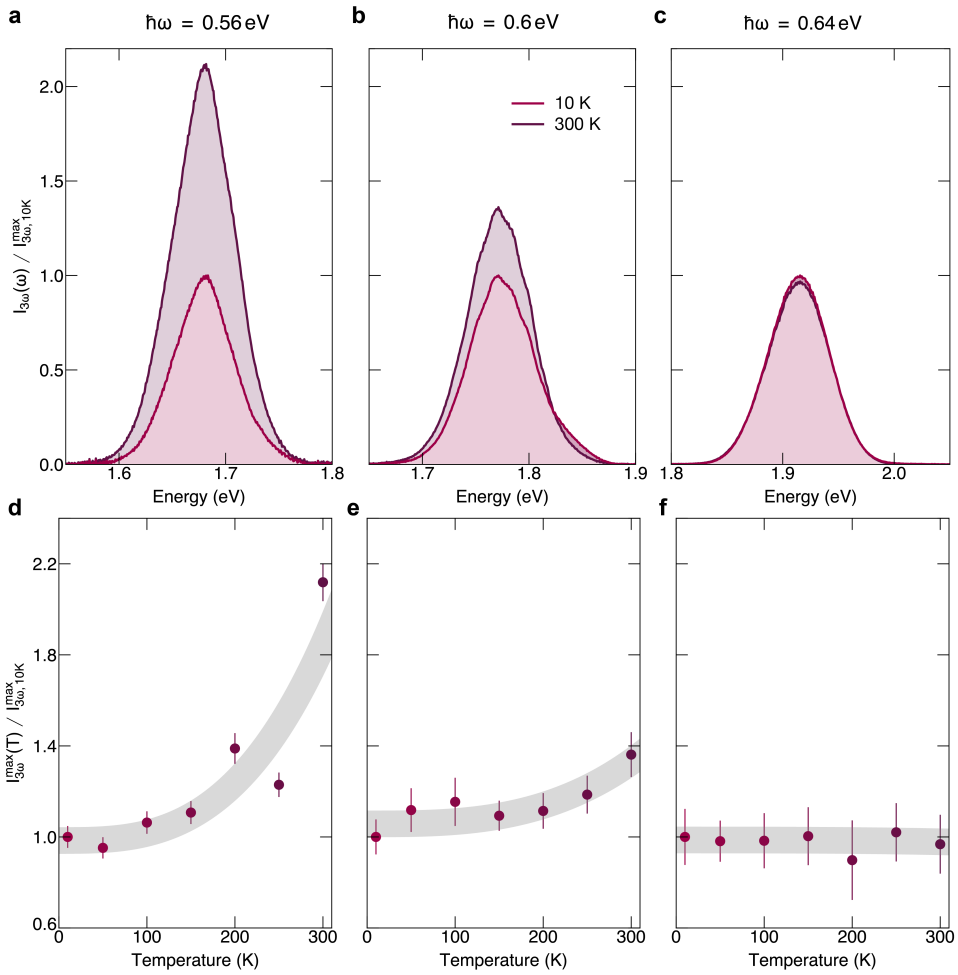

Fig. S10: Temperature dependence of the THG emission. a-c. Third harmonic spectra at equilibrium for selected NIR probe energies for the highest and lowest measured temperatures. The two temperatures corresponds to those compared in Ref. [4]. **d-f**. THG peak intensity intensity change as function of temperature and normalized to the THG emission at 10 K. Error bars are derived from repeated polarization scans and the grey line is a guide to the eye.

We cleave Sr_2CuO_3 crystals to expose a fresh *ab*-plane surface and mount them in a liquid-helium flow cryostat (LakeShore ST-100), which is immediately evacuated to high vacuum to prevent surface degradation. We perform THG measurements in a 45° reflection geometry at constant peak electric field for all sampled probe energies. For each photon energy, we acquire THG spectra from the same sample location by using a pair of cameras to correct for thermal drifts during cooldown and warm-up. To compensate for out-of-focus motion and maximize the THG signal, we adjust the sample position along the NIR propagation direction at every temperature point.

We then record two consecutive polarization-dependent angular scans while monitoring the THG signal with an Ocean Optics spectrometer, as described in the main text. We compare the datasets at the polarization yielding maximum THG intensity, i.e., along the chain axis. Owing to slight variations in beam pointing across infrared wavelengths, we cannot directly compare absolute THG intensities;

therefore, we normalize all spectra to the maximum intensity at 10 K for each wavelength. Figure S10a–c shows the normalized THG spectra at the highest and lowest measured temperatures, while Fig. S10d–f presents the temperature dependence of the normalized THG peak maxima. The THG intensity increases with temperature both below and at the exciton resonance, while remaining nearly constant above it. Across all measured near-infrared energies, the spectral shape remains essentially unchanged. This temperature-dependent behavior reflects the redshift of the absorption edge with increasing temperature and contrasts sharply with the Floquet-driven response: in the thermal case, the intensity at $\hbar\omega = 0.6$ eV *increases* due to the redshifting absorption edge, whereas it *decreases* under Floquet dressing (Fig. 4b-c of the main text). This qualitatively distinct behavior indicates that the transient modification of the THG signal cannot be simply explained in terms of a relative shift of the ground and excited states.

References

[1] in *Appendix G - Reflectance and Phase-Shift Dispersion Relations* (ed.Wooten, F.) *Optical Properties of Solids* 244–250 (Academic Press, 1972).

[2] Essler, F. H. L., Gebhard, F. & Jeckelmann, E. Excitons in one-dimensional Mott insulators. *Phys. Rev. B* **64**, 125119 (2001).

[3] Mitrano, M. *et al.* Pressure-Dependent Relaxation in the Photoexcited Mott Insulator ET − F_2TCNQ: Influence of Hopping and Correlations on Quasiparticle Recombination Rates. *Phys. Rev. Lett.* **112**, 117801 (2014).

[4] Kim, K. W., Gu, G. D., Homes, C. C. & Noh, T. W. Bound Excitons in Sr_2CuO_3. *Phys. Rev. Lett.* **101**, 177404 (2008).

[5] Neudert, R. *et al.* Manifestation of Spin-Charge Separation in the Dynamic Dielectric Response of One-Dimensional Sr_2CuO_3. *Phys. Rev. Lett.* **81**, 657–660 (1998).

[6] Sundaram, B. & Milonni, P. W. High-order harmonic generation: Simplified model and relevance of single-atom theories to experiment. *Phys. Rev. A* **41**, 6571–6573 (1990).

[7] Silva, R. E. F., Blinov, I. V., Rubtsov, A. N., Smirnova, O. & Ivanov, M. High-harmonic spectroscopy of ultrafast many-body dynamics in strongly correlated systems. *Nature Photonics* **12**, 266–270 (2018).

[8] Boyd, R. W. in *Chapter 3 - Quantum-Mechanical Theory of the Nonlinear Optical Susceptibility* Fourth edition edn, (ed.Boyd, R. W.) *Nonlinear Optics (Fourth Edition)* 137–202 (Academic Press, 2020).

[9] Gu, B. & Franco, I. Optical absorption properties of laser-driven matter. *Phys. Rev. A* **98**, 063412 (2018).

[10] Kishida, H. *et al.* Gigantic optical nonlinearity in one-dimensional Mott–Hubbard insulators. *Nature* **405**, 929–932 (2000).

[11] Mizuno, Y., Tsutsui, K., Tohyama, T. & Maekawa, S. Nonlinear optical response and spin-charge separation in one-dimensional Mott insulators. *Phys. Rev. B* **62**, R4769–R4773 (2000).

[12] Kishida, H. *et al.* Large Third-Order Optical Nonlinearity of Cu-O Chains Investigated by Third-Harmonic Generation Spectroscopy. *Phys. Rev. Lett.* **87**, 177401 (2001).

[13] Ogasawara, T. *et al.* Ultrafast Optical Nonlinearity in the Quasi-One-Dimensional Mott Insulator Sr_2CuO_3. *Phys. Rev. Lett.* **85**, 2204–2207 (2000).

[14] Lindblad, G. On the generators of quantum dynamical semigroups. *Communications in Mathematical Physics* **48**, 119–130 (1976).

[15] Gorini, V., Kossakowski, A. & Sudarshan, E. C. G. Completely positive dynamical semigroups of N-level systems. *Journal of Mathematical Physics* **17**, 821–825 (1976).

[16] Shan, J.-Y. *et al.* Giant modulation of optical nonlinearity by Floquet engineering. *Nature* **600**, 235–239 (2021).

[17] Sie, E. J. *et al.* Large, valley-exclusive Bloch-Siegert shift in monolayer WS_2. *Science* **355**, 1066–1069 (2017).